Kuwait J. Sci. **47 (1)** pp. 50-64, 2020

Computational algorithm of high-intensity focused ultrasound beams in cancer tissue model for hyperthermia therapy

Kittiphot Songkaitiwong, Kitsakorn Locharoenrat*

Dept. of Physics, Biomedical Physics Research Unit, Faculty of Science,
King Mongkut's Institute of Technology Ladkrabang, Bangkok 10520, Thailand
**Corresponding author: kitsakorn.lo@kmitl.ac.th*

Abstract

We calculate the acoustic field of a high-intensity focused ultrasound field in a 2D-model of human breast carcinoma and induce temperature elevation for the generation of necrosis. The computational operation is based on the Pennes bioheat concept. This method provides precise heat transfer values based upon thermal conduction in soft tissue and thermal convection in the domain of the blood. An ultrasound beam at 1 MHz was laterally focused on a tumor of 15.0 mm x 28.5 mm at different focal depths without elevational focalization. The length of each focus point of the ultrasound beam was 6.8 – 45.4 mm on the vertical axis, whereas the full width at half maximum was 1.1–2.5 mm on the horizontal axis. Simulated results showed that a discrepancy of the acoustic pressure around the focus area rises with focal depth. Like the pressure profile, when the focal depth is close to the ultrasound source, the thermal homogeneity around the focus area is attained, whereas thermal uniformity around the focus area becomes worse with increasing focal depth. Using the data visualization arrangement, a temperature profile corresponding to the obtained pressure profile is converted to attain a 2D image of a model of human breast carcinoma to show that tumor ablation was achieved and the healthy surrounding tissues were safe.

Keywords: Acoustic field; bioheat; cancer; hyperthermia; ultrasound.

1. Introduction

Human breast carcinoma is one of the most common fatal tumors. Thus, there is a concerted effort in the research community to understand these tumors (Newman *et al.,* 2015; Veronesi *et al.,* 2017). Many patients with breast carcinoma who are treated with typical medications, for instance chemotherapy, make few positive gains, partly due to diagnostic characteristics. High-intensity focused ultrasound treatment might be beneficial for local tumor control compared to traditional ultrasound therapy (Veronesi *et al.,* 2017). Therapy with high-intensity focused ultrasound is expected to benefit those whose symptoms progress and might turn to palliative care for breast carcinoma. High-intensity focused ultrasound uses the approach of non-invasive therapy for unresectable breast carcinoma. It can ablate the deep tissues surrounding the body via a high-intensity focused ultrasound beam from an external ultrasound source mask. Not only does it cause tissue necrosis differently than traditional ultrasound hyperthermia, it can also kill the tumors or suppress their growth. Furthermore, hyperthermia treatment through high-intensity focused ultrasound can achieve temperatures greater than 70 ^{o}C in the targeted tumor, causing cell destruction and necrosis in just a few seconds. Most patients suffering from breast carcinoma obtain significant relief from their discomfort after this therapy. It is suggested that high-intensity focused ultrasound treatment can be beneficial for localized tumor control. Therefore, it is expected that clinical use of high-intensity focused ultrasound treatment will open up a new generation of non-invasive local therapy. Also, high-intensity focused ultrasound treatment can become a viable therapy in the treatment of human breast carcinoma in the near future.

There have been many mathematical studies that seek to understand tumor dynamics. The Grünwald–Letnikov derivative was used to analyze the chemo response to an immunogenic tumor (Arshad *et al*., 2016). Local entropy was used to acquire a thermogram instead of a traditional mammogram in a human breast (Guzman-Cabrera *et al*., 2016). Caputo-Fabrizio with Mittag-Leffler kernel derivatives were used to obtain chaos in a cancer model (Gomez-Aguilar *et al*., 2017). The Caputo fractional operator alone was used to detect chemo and immune

responses to a tumor-obesity model (Yıldız *et al*., 2018). The Kernel fractional derivative was used to detect chemo and immune responses to the tumor-obesity model (Yıldız *et al*., 2018). Fractional operators Caputo and Caputo-Fabrizio were used to observe the immune response to a tumor-obesity model (Sadia Arshad *et al*., 2019).

Ultrasound hyperthermia in a cancer tissue model expressed by the conventional heat diffusion's equation has several concerning weak points. The traditional heat diffusion's equation is not well suited for describing the behavior of bioheat transfer in a soft biological tissue because the task considers only thermal conductivity and thermal diffusivity as a heat transfer. Furthermore, heat transfer with the two ultrasound beams is not one dimensional because the ultrasound beam has a three-dimensional beam and heating profiles. Therefore, the significance of this study is that we used the Pennes bioheat equation suitable for modeling bioheat, which is a far more complex phenomenon. Blood perfusion and metabolic heat sources are considered as well (Becker & Kuznetsov, 2014). Given the availability of modern software, we used a 2D model of a human breast carcinoma to model the effective hyperthermia therapy. The appropriate solution of Pennes bioheat equation was written in the two-coordinate system. The computational method of the five tissue layers in mimicking the tissue structure was established in healthy tissue and the tumor region with different parameters. The boundary conditions on the contact surface between the five tissue layers were considered. Owing to the pressure and temperature profiles via the tools of Matlab programming, data visualization allows us to observe the outcome of the high-intensity focused ultrasound on a clear image of the human breast carcinoma model.

2. Method of calculations

The ultrasound beam source is used to induce displacements of the acoustic medium via acoustic absorption. The direction of high-intensity focused ultrasound− induced cancer ablation is manipulated so that it is pointed against the focus area in an axial-direction. Because the lateral focus is without elevational focalization, the focus area is laterally small but broad along the vertical axis. Therefore, at a level of mechanical effect, this high ablation of high-intensity focused ultrasound is able to create the similar spatial thermal distribution. In order to model the finite-amplitude nonlinear wave propagation in the soft biological tissue, acoustic pressure (p) depends on input structures from tissue media and is calculated as follows:

$$\frac{\partial u}{\partial t} = -\frac{1}{\rho_0}\nabla p \tag{1}$$

$$\frac{\partial \rho}{\partial t} = -\left(2\rho + \rho_0\right)\nabla \cdot u - u \cdot \nabla \rho_0 \tag{2}$$

$$p = c_0^2\left(\rho + \mathrm{d}\cdot\nabla\rho_0 + \frac{B}{2A}\frac{\rho^2}{\rho_0} - \mathrm{L}\rho\right) \tag{3}$$

$$\mathrm{L} = -2\alpha_0 c_0^{y-1}\cdot\frac{\partial}{\partial t}\left(-\nabla^2\right)^{0.5y-1} 2\alpha_0 c_0^{y}\tan\left(0.5\pi y\right)\left(-\nabla^2\right)^{0.5(y-1)}, \tag{4}$$

where u is particle velocity, p is pressure amplitude, ρ is medium density, ρ_0 is ambient density (1 kg/m^3), c_0 is the sound of speed in the air (1,235 km/h), d is particle displacement, and B/A is the nonlinearity parameter caused by the finite-amplitude response to the sound speed. L is the linear intergo-differential operator responsible for acoustic absorption.

Combined Eqs. (1)-(3) describe the momentum, mass and energy within the soft biological tissue, giving us the generalized form of the second-order wave equation (Treeby *et al*., 2011).

When the thermal parameters are defined, the soft biological tissue is treated as a sound-absorbing fluid in which the absorption proceeds a law of power of frequency as

$$\alpha = 2\alpha_0 \pi f^{y}, \tag{5}$$

where α is absorption, and α_0 is the power law absorption coefficient. y is the power law exponent. f is the frequency of the ultrasound source.

Now the ultrasound heat deposition (Q) is calculated by (Grisey *et al*., 2016):

$$Q = \frac{\alpha\left(p\right)^2}{\rho_0' c}. \tag{6}$$

In general, the heat diffusion's equation is computed from (Chapra & Canale, 2015):

$$\rho' C_p \frac{\partial T}{\partial t} = K\nabla^2 T. \tag{7}$$

In our case, heat diffusion is modified according to Pennes bioheat equation as (Becker *et al*., 2014):

$$\rho' C_p \frac{\partial T}{\partial t} = K\nabla^2 T + q_m + q_p + Q. \tag{8}$$

The second, third, and fourth terms on the right hand side of Eq. (8) indicate the metabolic heat, blood perfusion, and heat deposition, respectively. ρ' is medium density, C_p is medium specific heat, K is thermal conductivity, and T is tissue temperature. The ambient temperature of blood is initially considered to be 37 °C.

With the known heat deposition terms at every time step, the exact temperature values in the blood flow domain of the soft biological tissue are calculated as

$$\rho' C_p \frac{\partial T}{\partial t} = K\nabla^2 T + q_m + \left[\rho_b' C_{pb} W(T_a - T)\right] + Q \tag{9}$$

$$\frac{\partial T}{\partial t} = \frac{1}{\rho' C_p}\left\{K\nabla^2 T + q_m + \left[\rho_b' C_{pb} W(T_a - T)\right] + Q\right\}. \tag{10}$$

A detailed explanation of the solution procedure is available in Newman & Bensenhaver (2015).

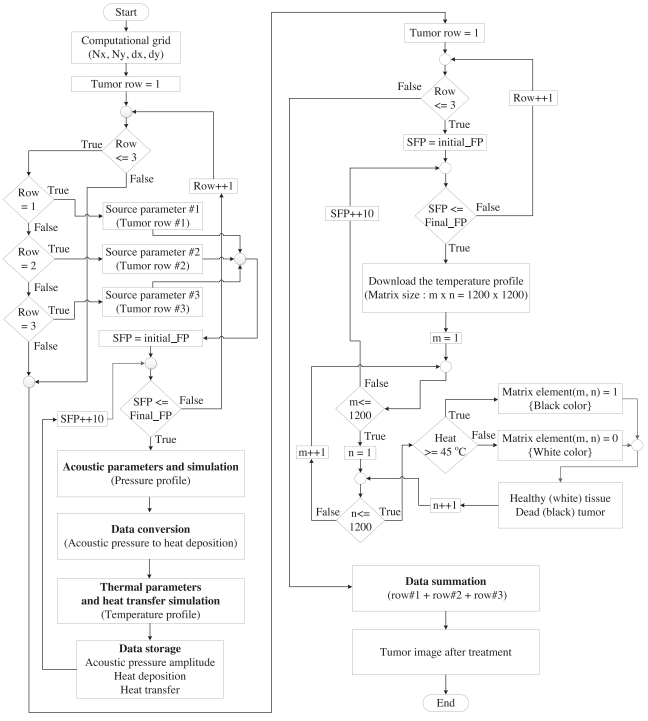

Fig. 1. Flow chart of the computational method in the 2D model of human breast carcinoma treated by the high-intensity focused ultrasound beam. SFP denotes the space of each focusing point.

The flow chart of the computational program in the human breast carcinoma model treated by the high-intensity focused ultrasound beam was presented in Figure 1. The 2D problem is analyzed using the available simulation k-wave software (Figure 2) (Treeby *et al.*, 2019). Simulation functions were commanded with five input structures to calculate the wave field propagation in the 2D model of the human breast carcinoma. The structures are grids, source, medium, sensor, and heat. Simulation properties are thus established as the fields for these input structures. These five structures are used to determine the details of the computational domain, acoustic source terms, acoustic medium, acoustic sensor point, and thermal medium. The goal is to record the progression of the pressure and corresponding temperature at each time step according to Eqs. (1) – (10). When the simulation functions were calculated, the wave field propagation in the defined medium was consequently simulated step-by-step and returned after a completion of the time loop of the simulation. The wave filed propagation at the sensor elements was simultaneously stored after the individual repetition.

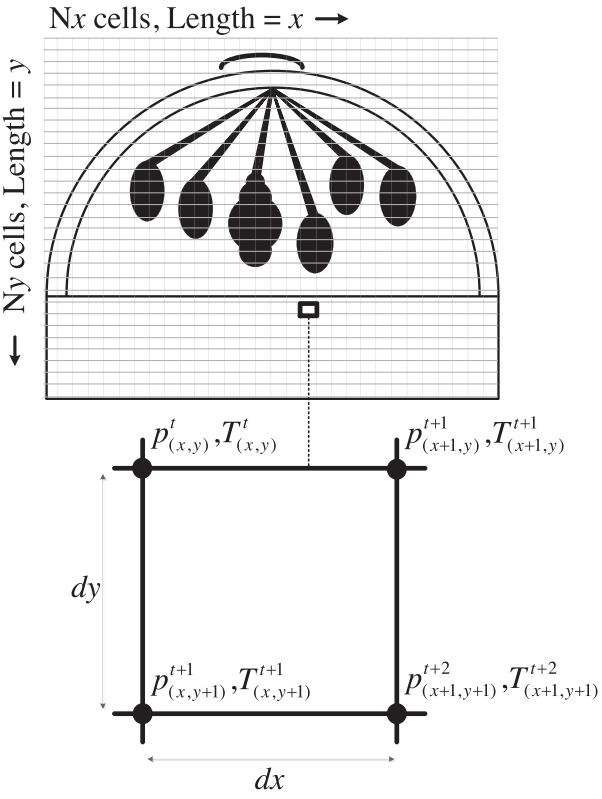

Fig. 2. Simulation procedures in a solution of the coupled first-order equation and Pennes bioheat equation by spatial (x,y) and temporal (t) grids for the 2D human breast carcinoma model.

The first input parameter is a computational domain created by 1200 x 1200 grid nodes in 2D human breast carcinoma. The grid node spacing is 100 μm. This indicates that the medium is separated into the uniformly distributed mesh of the grid nodes. The grid nodes indicate the discrete locations in a gap at which the manipulating equations are calculated. The function (makeGrid) makes

the pairs of inputs which conform to the number of grid nodes (N_x = 1200, N_y = 1200) and the grid node spacing (dx = 100 μm, dy = 100 μm) in every xy-direction. These variables are applied to construct the matrices of the k-wave numbers and grid coordinates. The k-wave numbers are applied to compute the spatial gradients of the acoustic wave field parameters via the Fast Fourier Transform library from the Matlab program. Maximum spatial frequency supported by a certain computational grid is defined by the Nyquist limit of two grid nodes per wavelength, whereas the maximum wave number corresponds to the maximum temporal frequency.

The second input parameter is to define the initial pressure distribution of the ultrasound source in the shape of an arc with the function (makeArc) and pulse amplitude in the medium to transmit the ultrasound signal at any particular time as shown in Table 1. By default, the initial pressure is spatially continuous in the simulation functions before running the simulation. The frequency and pulse of the ultrasound beam source are fixed at 1 MHz and 0.2 MPa, respectively (Zhou, 2015). Since the transmission energy rises with the increase in the radius of curvature up to the saturation level, the maximum radius of curvature is kept at 5 mm. However, at each focal depth, the aperture is fixed at 4 mm because this value is the maximum limit of energy transmission in the present study. There are three rows of focus area in the tumor. The first area is composed of nine focusing points starting at row #1 from left to right (1-9 positions). In addition, the second area is composed of fifteen focal points and begins at row #2 from left to right (1-15 positions). Lastly, the third area is composed of nine focusing points, beginning at row #3 from left to right This is similar to the positions of row 1 (1-9 positions).

The third input parameter is to define the geometrical structures of the medium as illustrated (Figure 3). First, the intermingling of fat, mammary glands, and tumors are determined. There are five similar orientations of mammary glands and six different orientations of milk ducts. The size of each mammary gland is 10.0 mm x 21.0 mm. The radius of the lobular structure of fat is 40 mm. The size of the tumor in the first stage of tumor growth with surface expansion and folding is 15.0 mm x 28.5 mm. The thickness of the skin and muscle layers are 3 mm and 50 mm, respectively. All functions are detailed in a k-wave toolbox for the construction of any geometric shapes that function (makeDisc, makeLine) for mammary glands and (makeDisc) for fat. Next, the properties of the medium in the individual grid nodes are defined (Table 2). There are four material properties to be specified: isotropic sound speed, ambient mass density, nonlinearity parameter, and power law absorption coefficient. It is noted that if the acoustic absorption is not established, the maximum sound speed within the acoustic medium would be required.

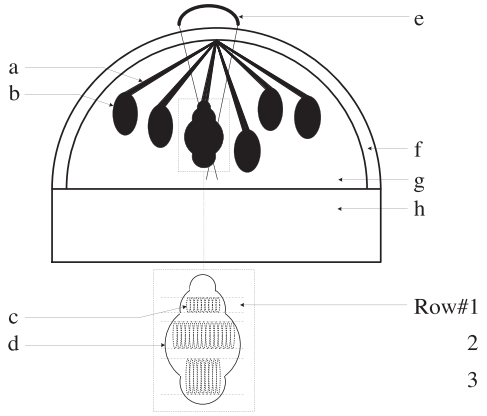

Fig. 3. Simulation model of the human breast carcinoma treated by the high-intensity focused ultrasound beam. a = milk duct, b = mammary gland, c = tumor area, d = focusing area, e = acoustic source mask, f = skin, g = fat, and h = muscle

Table 1. Properties of the high-intensity focused ultrasound source input structures.

Tumor row#	Ultrasound frequency [MHz]	Ultrasound pulse [MPa]	Focusing lens		Number of focal points	Space of each focal point, SFP [mm]
			Aperture size [mm]	Radius of curvature [mm]		
1	1.0	0.2	4.0	3.5	9	1.0
2	1.0	0.2	4.0	4.5	15	1.0
3	1.0	0.2	4.0	5.0	9	1.0

Table 2. Properties of the acoustic medium input structures (IT'IS Foundation, 2019; Li *et al*., 2009).

Medium	Sound speed, c [m/s]	Ambient density, ρ [kg/m^3]	Nonlinearity parameter, B/A	Power law absorption coefficient, α [dB/(MHz.cm)]
Skin	1624	1109	0	1.84
Fat	1478	911	10.07	0.39
Gland	1510	1041	9.63	0.88
Tumor	1548	920	7.17	1.20
Muscle	1585	1090	7.17	0.63

Table 3. Properties of thermal medium input structures (IT'IS Foundation, 2019; Gonzalez *et al*., 2007).

Medium	Heat diffusion			Blood perfusion			Metabolic heat, q_m [W/m^3]
	Density, ρ' [kg/m^3]	Specific heat, C_p [J/(kg.K)]	Thermal conductivity, K [W/(m.K)]	Density, ρ'_b [kg/m^3]	Specific heat, C_{pb} [J/(kg.K)]	Perfusion rate, W [1/s]	
Skin	1109	3391	0.37	-	-	-	-
Fat	911	2348	0.21	-	-	-	-
Gland	1041	2960	0.33	1043	3825	0.00018	450
Tumor	920	3000	0.42	1060	3167	0.00900	29000
Muscle	1090	3421	0.49	1043	3825	0.00018	450

The fourth input parameter is to define the ultrasound sensor array of 1200 x 1200 sensor grid nodes within the domain to receive and record the wave field propagation at the individual sensor node for each time step while running the simulation. Most of the ultrasound source terms are kept at the ultrasound sensor points for every time step.

The final input parameter is to define the thermal medium as detailed in Table 3. The first layer is skin and the last is muscle. A constant temperature of 37 °C is defined at the skin layer. Thermal boundary condition #1 is set at 37 °C for all normal tissues, whereas the thermal boundary condition #2 is set to $45\,^{\circ}\mathrm{C} \le T < 46\,^{\circ}\mathrm{C}$ in order to kill all cancerous cells without damaging the surrounding normal tissues.

After the five input parameters are defined, the simulation functions can be programmed. The whole values of the acoustic pressure and corresponding temperature at the sensor points are stored at individual time steps while the simulation is running. Finally, the outputs for these parameters are indexed. Lastly, the output data that is reloaded into Matlab copies the acoustic sensor data from the input to the output file when the simulation is completed. This allows us to visualize the output file in post-processing.

To show the overall image of the human breast carcinoma model, the elements (x,y) = 1 within the display mask are changed to black within the display, representing the dead tumor. In contrast, elements (x,y) = 0 within the display mask are changed to white within the display, representing the healthy tissue. This is based on the following boundary conditions: (1) the temperature of the high-intensity focused ultrasound beam can destroy a tumor at 45 °C without damaging normal tissue, (2) the thermal boundary condition #2 is set to $45\,^{\circ}\mathrm{C} \le T < 46\,^{\circ}\mathrm{C}$ to kill all cancerous cells, and (3) the thermal boundary condition #1 is set to T = 37 °C for normal tissue. Therefore, a summation of all matrix elements gives us the overview of the image of the 2D simulation model. A detailed description of the Matlab code is available in the supplementary information file.

3. Results and discussion

A 2D-simulation model using a high-intensity ultrasound source for the effective hyperthermia treatment is carried out by constructing the suitable ultrasound source, medium, and sensor input structures. The frequency of the ultrasound source was fixed at 1 MHz with a fractional bandwidth of 100%. The focal plane is defined at three different levels of focal depths (row #1-3 in Figure 3). Human breast carcinoma structures, dimensions, and compositions at the different layers and cross sections were then designed. Mesh dependence was performed by comparing the pressure and temperature profiles in the final working mesh with the pressure and temperature data attained in a refined mesh. For the calculation of acoustic pressure and temperature profiles in the breast carcinoma model, the simulation domain had dimensions of 120 mm x 120 mm. The number of grids was 1200 x 1200. The treatment time of approximately 26 min sufficed for the simulation. The sensor array was calculated within a 1200 x 1200 grid point spacing, corresponding with the simulated 2D array ultrasound source mask that consisted of N_x x N_y = 1200 x 1200 grid points with an element pitch of dx x dy = 100 μm x 100 μm. This ensured the accuracy of the simulation. The refined grids around the focus area were also generated with a mesh size of 100 μm x 100 μm.

Next, the human breast tissue structure, including the tumor area of 15.0 mm x 28.5 mm, was excited by the high-intensity focused ultrasound source used to detect the treated cancerous cells. Pressure wave fields within each tissue cross section were calculated according to the first order simulation in Eqs. (1)-(4). After completion of the simulation, the propagation of the field was displayed in Figures. 4-5. It was observed that the human breast tissues with tumors and those without tumors have a difference in wave field propagation. They are shown at three different levels of the focus area aligned in a focal plane (xy-position) attributable to the different three focal depths along the y-position.

The high-intensity focused ultrasound pulse of +/- 0.2 MPa in amplitude at the human breast carcinoma model is illustrated in Figure 4. Figure 4 shows the evolution of the wave front indicates a mechanism for the formation of specific features appearing in the received wave front. The simulated internal wave front in rows #1-3 aligns closely with a main direction of pressure wave field propagation during the initial propagation through the skin, fat, gland, and muscle tissue, respectively. The distinctive feature of this portion of the wave field propagation introduces the large-scale time-shift fluctuation caused by the pressure wave field propagation through the lobular structure of fat. Since the fat has a lower sound speed than the other four media, the propagation through this area caused the dispersion of the wave front. This dispersion accumulated as the wave field further propagated through the fat layer. A portion of the wave front was then refracted. The accumulated refraction was also strongly visible in the wave front after propagation through the muscle structure. Thus, the time-shift aberration occurring in this tissue model is thought to be a variation of sound speed and irregularity of the interfaces between the tissue layers. This result agrees with research by Treeby *et al*. (2012).

Figure 5 shows the acoustic pressure in the human breast carcinoma model caused by the ultrasound pulse from Figure 4. Here one can see that the amplitude of the acoustic pressure is more intense in the vicinity of the ultrasound source mask, showing significant absorption by the breast carcinoma structure. During pressure field propagation, the amplitude of the acoustic pressure is attenuated due to the multiple reflections across various media from the breast tissue compositions. Furthermore, the clear existence of the tumors prevents the propagation of the ultrasound waves and behaves like an electric wall with a strong decrease in amplitude of the transmitted signal. In addition, due to a difference of the radius of curvature in the focusing lens, the distribution uniformity of the acoustic pressure at the different focus area is clearly observed. As the focal depth rises, the contour uniformity of the acoustic pressure becomes poor. The contour map of each focal point is 6.8 – 45.4 mm in length along the y-position, and 1.1 – 2.5 mm in the full width at half maximum along the x-position. This uniformity of the acoustic pressure in Figure 5 corresponds with the fluctuation of the ultrasound pulse around the focus area in Figure 4.

Ultrasound heat deposition was determined according to Eqs. (5) – (6). Temperature profiles within individual tissue cross sections were calculated according to Pennes bioheat concept in Eqs. (8) – (10). They are displayed at different levels of focus area aligned in a focal plane

(xy-position) with three different focal depths along the y-position (see Figures 6 & 7). Figure 6 clearly shows the heat deposition as a result of the magnitude of a large-scale time-shift and amplitude fluctuation It also shows the presence of waveform distortion visibly observed from Figures 4 and 5. A simulated internal heat wave was used in rows 1-3 aligned apart from the main direction of heat wave propagation during the propagation through skin, fat, gland, and muscle tissue, respectively. The results show the cumulative formation of thermal fluctuations by dispersion at the fat-tumor interface (Figure 7). As the heat wave propagates along a path that includes the tumor cells, heat energy is scattered outside the main direction of the propagation. Scattered energy positively interacts in a manner determined by the angle and contrast of the tumor cells. The secondary waveform is thus revealed by the heat transfer profile. Since the transmitted heat pulse had the short temporal duration (broad band), scattering from the fat-tumor interface lead to the removal of energy from the main waveform, causing heat dropouts in the received waveform. This effect is inherently different from effects of coherent interference that may occur for narrow band propagation through soft biological tissue. Therefore, the heat transfer profile clearly shows the multiple scattering effects; for instance, a secondary waveform is caused by scattering at the fat-tumor interface. It would be further scattered and distorted in the propagation path. These outcomes result in the random heat wave that appears behind the principal waveform. The result is that as the focal depth is near the ultrasound source, a relatively small length of focus area is obtained with an acceptable uniformity level. The uniformity becomes worse when the focal depth increases. As the focal depth increases further, the focus area tends to divide into two-subregions. The contour map of each focusing point is 3.5–9.3 mm in length along the y-position and 0.7–1.9 mm in the full width at half maximum along the x-position. Furthermore, the temperature stability at the blood-tissue interface is confirmed by the consolidate heat-transfer issue. The condition of the boundary between the medium interface is determined in light of the thermal conduction in the soft tissue domain and thermal convection in the blood vessel domain.

After the temperature profile of the human breast carcinoma is finally simulated according to Eq. (10), the tumor can be identified by the thermal difference as shown in Figure 8. Each temperature profile conforms to a defined focusing lens and focal length. Interpolation of the maximum gains and conforming depths across all profiles are used to achieve the high-intensity focused ultrasound– induced cancer ablation with heat tapping of the 2D-tissue model. Output data reloaded into Matlab reproduces the sensor data from the input file to the output at the end of the simulation. This helps in post-processing and visualization of the outputs. Element (x,y) = 1 within the display mask is identified as black in the display, whereas element (x,y) = 0 is identified as white. Elements concerned with 1 will represent the dead tumor, whereas elements concerned with 0 will display healthy tissue at each grid node. Based on the thermal boundary conditions 1 and 2, the thermal boundary condition #1 is set to $T = 37$ ^{o}C for normal tissue, while the thermal boundary condition #2 is set to $45\,^{\circ}\mathrm{C} \le T < 46\,^{\circ}\mathrm{C}$ to kill all cancerous cells. The summation of all matrix elements offers the overview of the image of the 2D-simulation model. Data visualization suggests that the hyperthermia treatment could destroy the cancerous cells without causing additional complications.

At the level of biological effect, high-intensity ultrasound results in tissue heating and necrosis, cell apoptosis, and cell lysis. Coagulation necrosis appears in the tissues exposed to high-intensity focused ultrasound as the temperature of the tissue is increased to a particular level for a certain time. Furthermore, though most initial cell death in tissues exposed to high-intensity focused ultrasound is caused by cell necrosis from thermal injury, high-intensity focused ultrasound is able to induce apoptosis. Nonlinear effects observed from the high-intensity focused ultrasound beam result in quicker attenuation of the ultrasound energy and quicker tissue heating. Ablated tumors caused by cell necrosis and apoptosis increase the cell destruction. In summary, the response of high-intensity focused ultrasound for effective hyperthermia treatment is thought to have thermal, mechanical, and biological effects. The next step towards best practices is a comparative study on previous dual beam ultrasound research and this current high-intensity focused study.

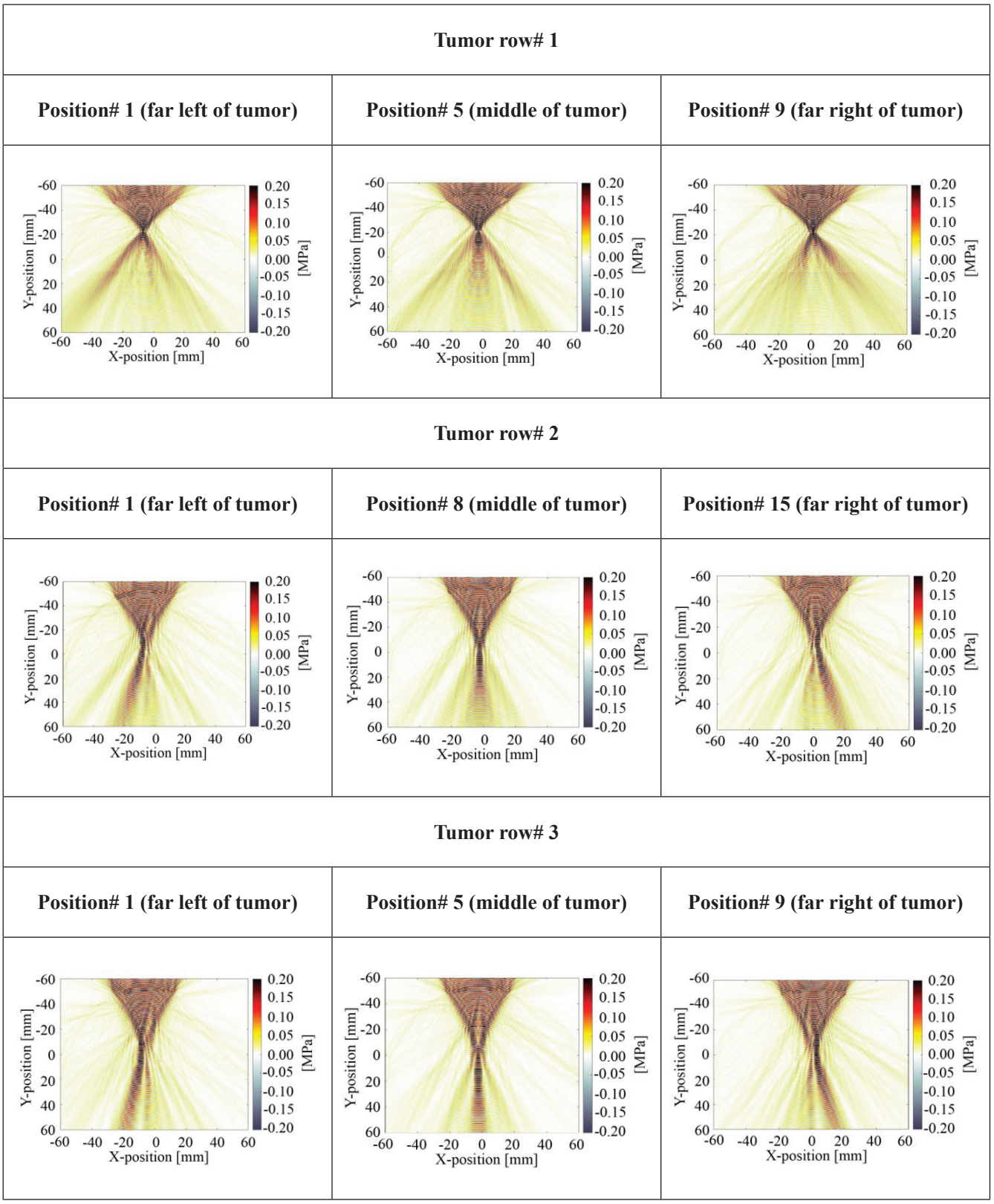

Fig. 4. 2D-simulation of a high-intensity focused ultrasound pulse at the amplitude of +/- 0.2 MPa in the human breast carcinoma model with a specified tumor size = 15.0 mm x 28.5 mm. The k-wave color map represents the positive pressures as yellow-red-black and negative pressures as light-grey. The ultrasound source mask is displayed as a black line.

Tumor row# 1		
Position# 1 (far left of tumor)	**Position# 5 (middle of tumor)**	**Position# 9 (far right of tumor)**
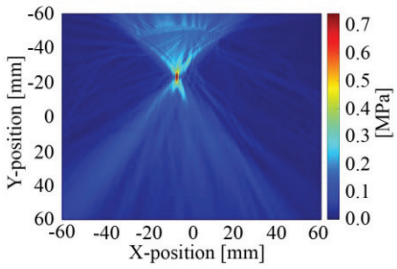	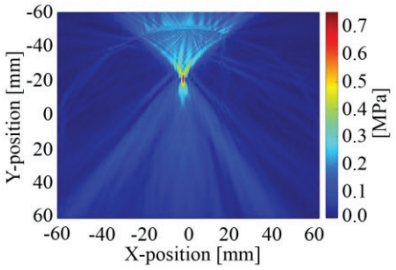	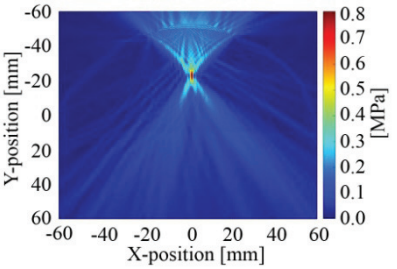
Tumor row# 2		
Position# 1 (far left of tumor)	**Position# 8 (middle of tumor)**	**Position# 15 (far right of tumor)**
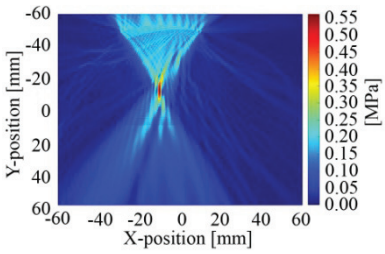	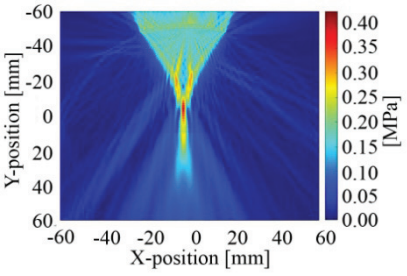	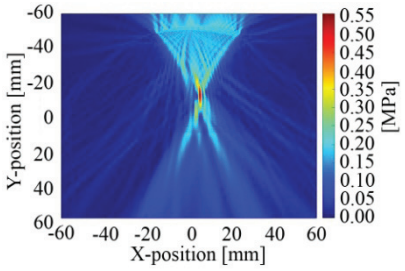
Tumor row# 3		
Position# 1 (far left of tumor)	**Position# 5 (middle of tumor)**	**Position# 9 (far right of tumor)**
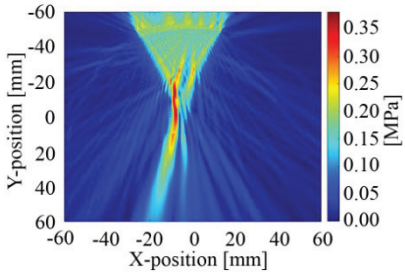	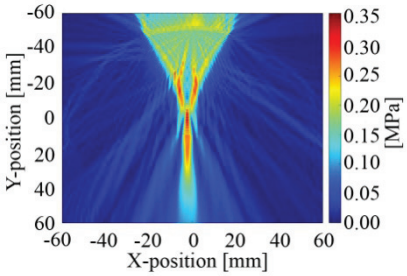	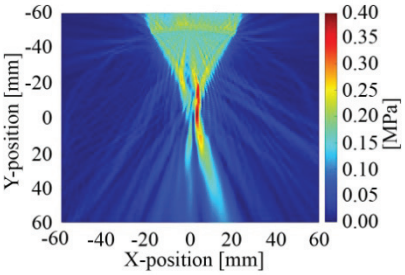

Fig. 5. Acoustic pressure (p) in the human breast carcinoma model treated by the high-intensity focused ultrasound beam.

Tumor row# 1		
Position# 1 (far left of tumor)	**Position# 5 (middle of tumor)**	**Position# 9 (far right of tumor)**
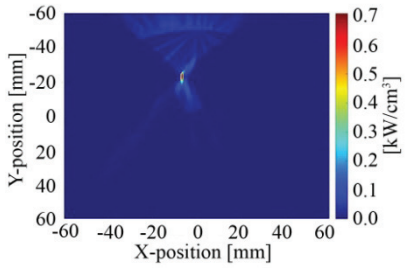	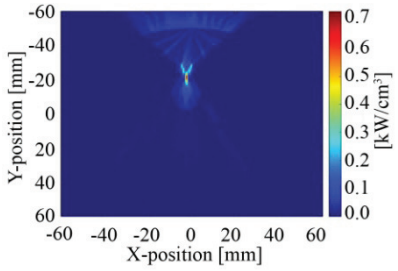	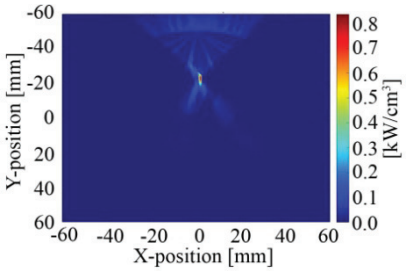
Tumor row# 2		
Position# 1 (far left of tumor)	**Position# 8 (middle of tumor)**	**Position# 15 (far right of tumor)**
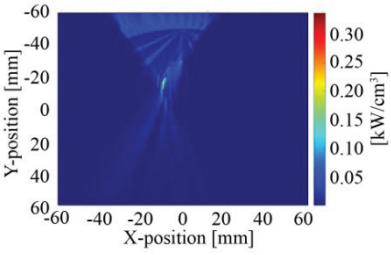	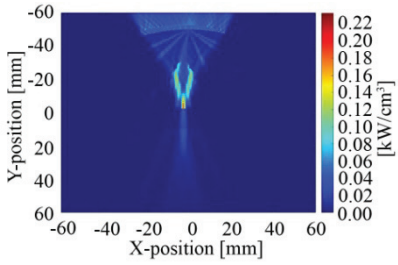	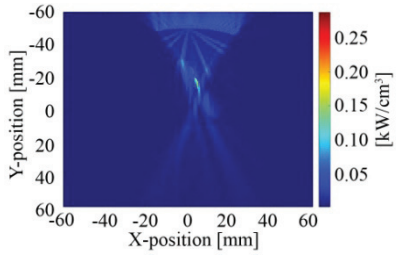
Tumor row# 3		
Position# 1 (far left of tumor)	**Position# 5 (middle of tumor)**	**Position# 9 (far right of tumor)**
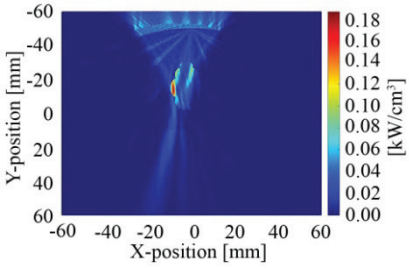	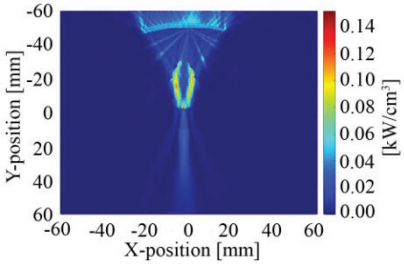	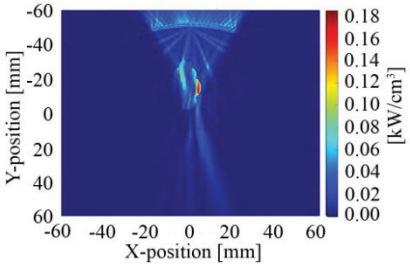

Fig. 6. Heat deposition (Q) in the human breast carcinoma model treated by the high-intensity focused ultrasound beam.

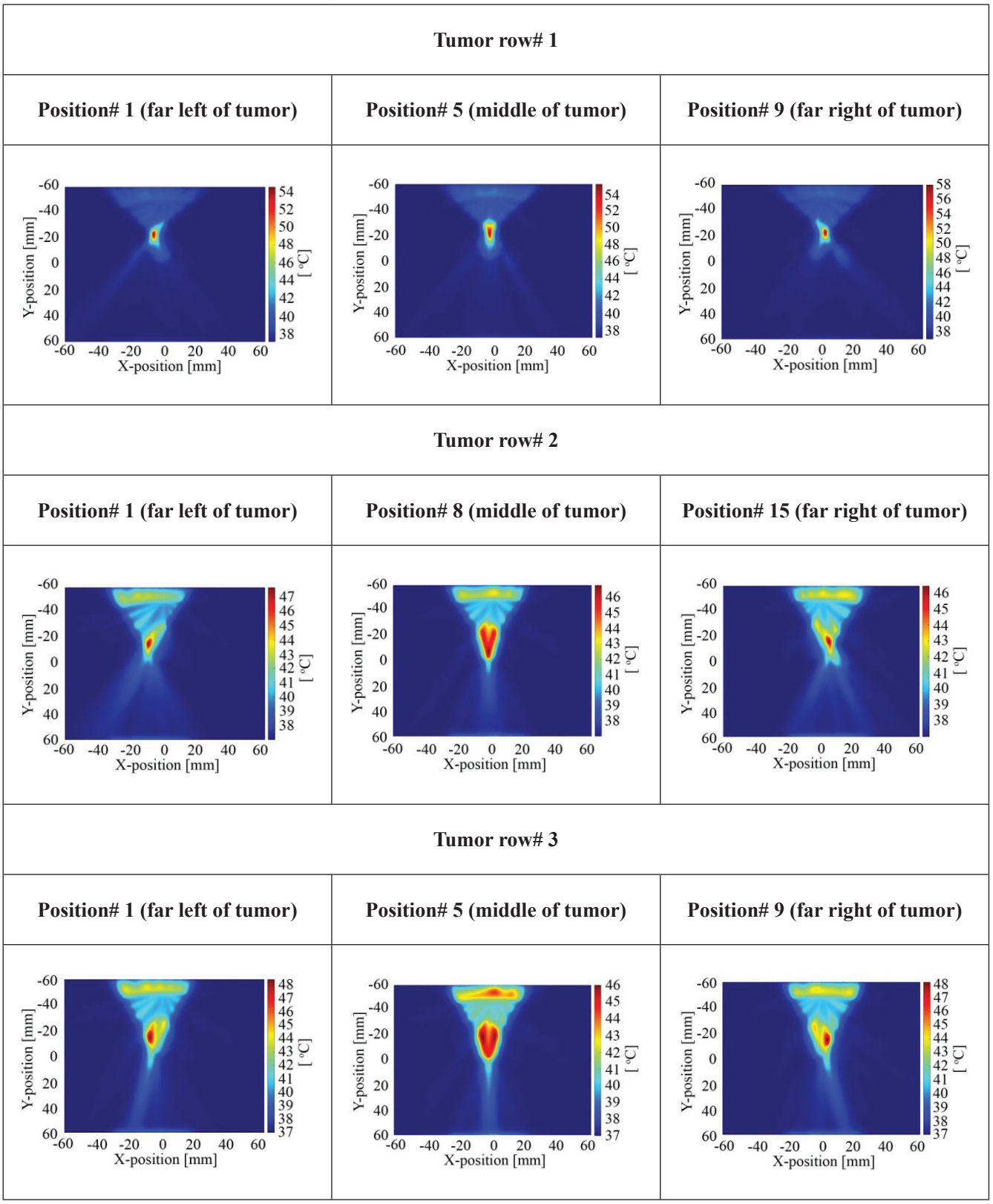

Fig. 7. Temperature profile in the human breast carcinoma model treated by the high-intensity focused ultrasound beam.

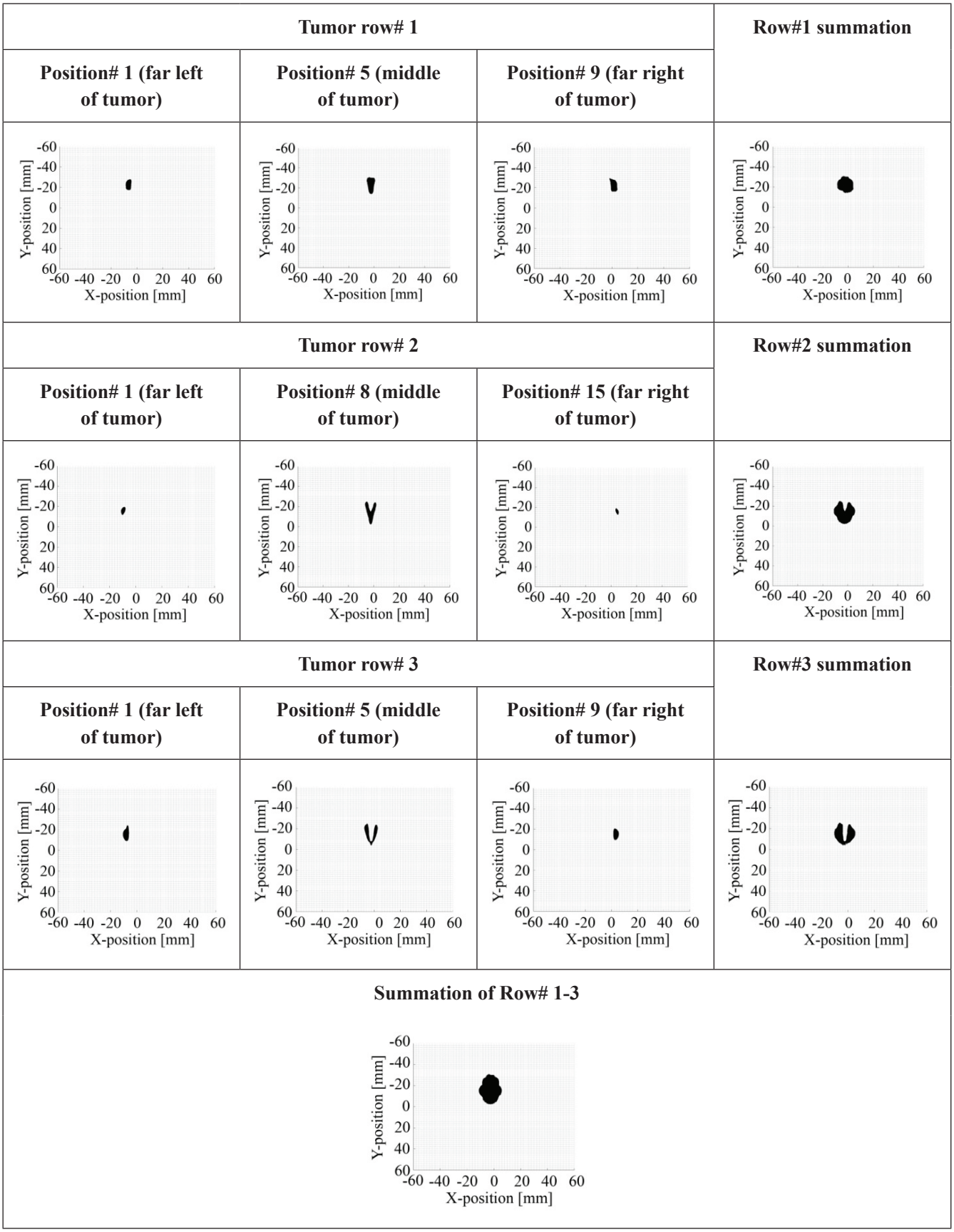

Fig. 8. Data visualization of the treated tumor size of 15.0 mm x 28.5 mm in the human breast carcinoma model after hyperthermia treatment by the high-intensity focused ultrasound beam.

4. Conclusions

Cancer ablation aiming to induce the displacement of 2D human breast carcinoma structures via high-intensity focused ultrasound at a frequency of 1 MHz was simulated by the Matlab program. This method is dependent on the Pennes bioheat equation, which offers a more precise heat transfer calculation based on the ultrasound source and thermal parameters in the acoustic medium from the 2D tissue model. Each focal point of the ultrasound beam lies in the focal plane with a length of 6.8 – 45.4 mm along the vertical axis, while the full width at the half maximum is 1.1 – 2.5 mm along the horizontal axis. Simulated results have shown that the excitation of the ultrasound source introduces the distribution uniformity of the acoustic pressure in a tumor with a size of 15.0 mm x 28.5 mm. The pressure conversion to heat deposition gives the temperature profile. Similar to the pressure profile, a deviation of the ultrasound temperature around the focus area increases when the focal depth increases until reaching the muscle area. When the focal depth is relatively close to the ultrasound source, the uniformity of the ultrasound temperature around the focal area reaches a satisfactory level. However, this uniformity is poor as the focal depth increases. The precise temperature values are therefore manipulated to attain the data visualization of the 2D-model of the complete ablated tumor as compared with the normal tissue within a safety margin, indicating the effectiveness of hyperthermia therapy.

ACKNOWLEDGEMENTS

This research was funded by King Mongkut's Institute of Technology Ladkrabang, Bangkok 10520, Thailand under a grant number KREF046206.

Ethics approval and consent to participate: Not applicable.

Conflict of interests: There are no conflicts of interest concerning this research.

Data Availability: Matlab code used for data supporting the conclusion of this study is included within the supplementary information file.

References

Arshad S., Baleanu, D., Haund, F. & Tang, Y. (2016). Dynamical analysis of fractional order model of immunogenic tumors. Advances in Mechanical Engineering, **8**(7): 1-13.

Arshad, S., Baleanu, D., Defterli, O. & Shumaila, A. (2019). Numerical framework for the approximate solution of fractional tumor-obesity model. International Journal of Modeling Simulation Science and Computing, **10**(1): 1941008.

Becker, S. & Kuznetsov, A. (2014). Heat transfer and fluid flow in biological processes, Academic Press, New York, Pp. 55-97.

Chapra, S.C. & Canale, R.P. (2015). Numerical methods for engineers, Mc Graw Hill, New York, Pp. 11-25.

Gomez-Aguilar, J.F., Lopez-Lopez, M.G. & Alvarado-Martinez, V.M. (2017). Chaos in a cancer model via fractional derivatives with exponential decay and Mittag-Leffler Law. Entropy, **19**(12): 681.

Gonzalez, F.J. (2007). Thermal simulation of breast tumor. Revistra Maxixana De Fesica, **53**(4): 323-326.

Grisey, A., Yon, S., Letort, V. & Lafitte, P. (2016). Simulation of high-intensity focused ultrasound lesions in presence of boiling. Journal of Therapeutic Ultrasound, **4**: 11.

Guzman-Cabrera, R., Guzman-Sepulveda, J.R., Parada, A.G. & Garcia, J.R. (2016). Digital processing of thermographic images for medical applications. Revista De Chimie, **67**(1): 53-56.

IT'IS Foundation (2019). Database at a Glance, https://itis.swiss/virtual-population/tissue-properties/database/ (accessed 01 Jan 2019).

Li, C., Littrup, P. & Huang, L. (2009). In vivo breast sound-speed imaging with ultrasound tomography. Ultrasound in Medical Biology, **35**(10): 1615-1628.

Newman, L.A. & Bensenhaver, J.M. (2015). Ductal carcinoma in-situ and microinvasive/borderline breast cancer, Springer, Heidelberg, Pp. 22-30.

Treeby, B., Cox, B. & Jaros, J. (2019). A Matlab toolbox for the time-domain simulation of acoustic wave fields, http://www.k-wave.org/ (accessed 01 Jan 2019).

Treeby, B.E., Jaros, J., Rendell, A.P. & Cox, B.T. (2012). Modeling nonlinear ultrasound propagation in heterogeneous media with power law absorption using a k-space pseudospectral method. Journal of Acoustic Society of America, **131**(6): 4324-4336.

Treeby, B.E., Tumen, M. & Cox, B.T. (2011). Medical image computing and computer-assisted intervention, Springer, Heidelberg, Pp. 67-80.

Veronesi, U., Goldhirsch, A., Veronesi, P., Gentilini, O.D. & Leonardi, M.C. (2017). Breast cancer: Innovations in research and management, Springer, Heidelberg, Pp. 37-45.

Yıldız, T.A., Arshad, S. & Baleanu, D. (2018). New observations on optimal cancer treatments for a fractional tumor growth model with and without singular kernel. Chaos, Solitons & Fractals, **117**: 226-239.

Yıldız, T.A., Arshad, S. & Baleanu, D. (2018). Optimal chemotherapy and immunotherapy schedules for a cancer-obesity model with Caputo time fractional derivative. Mathematical Method Applied Science, **41**(18): 9390-9407.

Zhou, Y. (2015). Principles and applications of therapeutic ultrasound in healthcare, CRC Press, New York, Pp. 102-110.

Submitted : 13/05/2019

Revised : 23/07/2019

Accepted : 30/07/2019

خوارزمية حسابية لشعاع الموجات فوق الصوتية عالية الكثافة في نموذج الأنسجة السرطانية لعلاج ارتفاع الحرارة

كيتيفوت سونجكايتيونج، كيتساكورن لوكارونات
وحدة أبحاث الفيزياء الطبية الحيوية، قسم الفيزياء، كلية العلوم،
معهد الملك مونغكوت للتكنولوجيا، بانكوك، تايلاند

الملخص

نقوم بحساب المجال الصوتي لحقل الموجات فوق الصوتية المركزة عالية الكثافة في نموذج ثنائي الأبعاد لسرطان الثدي البشري وارتفاع درجة الحرارة المستحث لتوليد النخر. وتستند العملية الحسابية على مفهوم الحرارة الحيوية بينز. توفر هذه الطريقة قيم دقيقة لنقل الحرارة تعتمد على التوصيل الحراري في الأنسجة الرخوة وانتقال الحرارة في الدم. شعاع الموجات فوق الصوتية عند 1 ميغاهيرتز يركز أولاً على ورم بحجم 15.0 مم × 28.5 مم في أعماق مركزية مختلفة دون التركيز البؤري. يتراوح طول كل نقطة بؤرية لحزمة الموجات فوق الصوتية بين 6.8 و45.4 ملم في المحور العمودي، في حين أن العرض الكامل بنصف الحد الأقصى هو 1.1– 2.5 ملم في المحور الأفقي. وأظهرت نتائج المحاكاة أن التباين في الضغط الصوتي حول منطقة التمركز يرتفع بعمق بؤري. مثل ملف الضغط، عندما يكون البعد البؤري قريباً من مصدر الموجات فوق الصوتية، يتم تحقيق التجانس الحراري حول منطقة التمركز، في حين أن التماثل الحراري حول منطقة التمركز يصبح أسوأ مع زيادة البعد البؤري. وباستخدام نظام مؤثرات عرض البيانات، يتم تحويل ملف تعريف درجة الحرارة المطابق لملف الضغط الذي تم الحصول عليه للوصول إلى صورة ثنائية الأبعاد لنموذج سرطان الثدي البشري لإظهار أنه تم استئصال الورم وأن الأنسجة السليمة المحيطة آمنة.